



# Numerical Analysis on the Spatiotemporal Characteristics of the Portevin–Le Chatelier Effect in Ti-12Mo Alloy

Shiyuan Luo<sup>1,2</sup> · Yongxin Jiang<sup>1,2</sup> · Sandrine Thuillier<sup>3</sup> · Philippe Castany<sup>4</sup> · Liangcai Zeng<sup>1,5</sup>

Received: 25 January 2022 / Accepted: 12 April 2022 / Published online: 4 June 2022  
© The Author(s) under exclusive licence to The Korean Institute of Metals and Materials 2022

## Abstract

A simplified 3D FE model based on McCormick's model is developed to numerically predict the spatiotemporal behaviors of the PLC effect in Ti-12Mo alloy tensile tests at 350 °C with strain rates from the order of  $10^{-4} \text{ s}^{-1}$  to  $10^{-2} \text{ s}^{-1}$ . The material parameter identification procedure is firstly presented in details, and the simulated results are highly consistent with experimental ones, especially in terms of stress drop magnitudes and PLC band widths. The distribution of simulated stress drop magnitudes at a constant tensile velocity (0.01 mm/s) follows a normal distribution and its peak value is in the range of 26–28 MPa. Furthermore, the simulated band width slightly fluctuates with the increase of true strain and its average value is about 1.5 mm. Besides, the staircase behavior of strain–time curves and the hopping propagation of the PLC band are observed in Ti-12Mo alloy tensile process, which are related to the strain localization and stress drop magnitudes.

**Keywords** Ti-12Mo alloy · Portevin–Le Chatelier effect · Spatiotemporal behaviors · FE modeling

## 1 Introduction

Titanium alloys are extensively used in numerous areas from aeronautics to biomedical devices, due to their high strength-to-weight ratio, good corrosion resistance and excellent biocompatibility [1–3]. Hereinto, metastable  $\beta$  Ti-xMo alloys synthesized by nontoxic elements are regarded as ones of promising metallic orthopedic implant materials [4–7]. However, according to previous studies, a type of plastic instability, namely Portevin–Le Chatelier (PLC) effect, is observed in Ti-xMo alloys under various thermo-mechanical

loading conditions [8–10]. Therefore, to accurately predict the spatiotemporal behaviors of the PLC effect in Ti-xMo alloys is of great importance for the process optimization and practical application of these materials.

The PLC effect exhibits itself as serrated flow in stress–strain curves and localized deformation bands in specimens of metallic alloys [11]. Until now, some researches have been performed on the PLC effect from temporal and spatial aspects. Focusing on the former, Chihab et al. [12] and Amokhtar et al. [13] respectively investigated the influence of strain rates and alloying element contents on stress drop magnitudes in Al–Mg alloys, and experimental results indicated that the stress drop magnitude is negative correlation with strain rates and positive correlation with Mg contents. Moreover, Zhang et al. [14] studied stress drop magnitudes in Ni–Co superalloy tensile tests within the temperature range of 350–550 °C, and found that the stress drop magnitude increases when the temperature rises. Furthermore, Chen et al. [15] studied the effects of temperature and strain rate on the critical strain of the PLC effect in HfN-bTaTiZr high-entropy alloy, and discovered that unlike the normal behavior of strain rate effect, the evolution trend of critical strain transfers from a normal behavior to an inverse behavior as enhancing the temperature to a given value. On the other hand, for the spatial aspect, the PLC band propagation is classified as types A, B and C, which are respectively

✉ Shiyuan Luo  
shiyuanluo@wust.edu.cn

<sup>1</sup> Key Laboratory of Metallurgical Equipment and Control Technology, Ministry of Education, Wuhan University of Science and Technology, Wuhan 430081, China

<sup>2</sup> Hubei Key Laboratory of Mechanical Transmission and Manufacturing Engineering, Wuhan University of Science and Technology, Wuhan 430081, China

<sup>3</sup> Université Bretagne Sud, UMR CNRS 6027, IRDL, 56100 Lorient, France

<sup>4</sup> Université de Rennes, INSA Rennes, CNRS, ISCR-UMR 6226, 35000 Rennes, France

<sup>5</sup> Precision Manufacturing Institute, Wuhan University of Science and Technology, Wuhan 430081, China

continuous propagation, hopping propagation and random nucleation [16–18]. Mehenni et al. [19] compared the propagation characteristics of the PLC bands at different strain rates in Al–Mg alloys, and the results suggested that the propagation type of the PLC band transfers from type C to type B and eventually to type A when increasing the strain rate. Yu et al. [20] reported that the inclined angles of PLC bands range within 50–60° with respect to the tensile direction during the propagation process. Besides, some studies [21–23] were performed on quantitatively characterizing the variation of the PLC band width at different testing conditions. Note that, all of the aforementioned investigations are performed by experiments rather than finite element (FE) methods.

Focusing on the modeling of the PLC effect, a mathematical model is firstly developed by Kubin and Estrin [24], which is based on a macroscopic description of deformation bands. However, this model has difficulties in quantitatively describing the spatiotemporal characteristics of the PLC effect. Hence, according to a microscopic description of the dynamic strain ageing, McCormick [25] proposed another mathematical model, in which the negative strain rate sensitivity and serrations are implicit consequences of constitutive equations. Then, Zhang et al. [26] implemented McCormick's model in the Abaqus software as an external subroutine, and simulated the PLC effects of both flat and round specimens in Al–Mg–Si alloy tensile tests. Moreover, Mazière et al. [27] employed McCormick's model to analyze the temporal behavior of the PLC effect in nickel-based superalloy. Furthermore, Manach et al. [28] used McCormick's model to analyze the PLC effect in an Al–Mg alloy, and compared the simulated results with experimental ones in terms of stress drop magnitudes and propagation types of the PLC bands. Mansouri et al. [29] employed McCormick's model to predict the PLC effect of aluminium alloys in the case of room temperature Erichsen tests. Besides, considering the temperature effect, Belotteau et al. [30] improved McCormick's model by using temperature dependent material parameters. Mansouri et al. [31] and Moon et al. [32] utilized the improved McCormick's model to predict the PLC effect of aluminum alloys during tensile and simple shear as well as limiting dome height formability tests. Note that, although a large number of simulation works have been performed on the PLC effect in various metallic alloys, however, none of them is tied to the prediction of the PLC effect in Ti–Mo alloys.

Consequently, this paper is aimed to utilize FE method to investigate the spatiotemporal behaviors of the PLC effect in Ti–12Mo alloy. For this purpose, McCormick's model is employed and its material parameters are identified in details. Then, a simplified 3D FE model based on the calibrated McCormick's model is developed by using Abaqus 6.14 software and verified by experiments. Finally,

the spatiotemporal characteristics of the PLC effect in Ti–12Mo alloy tensile tests at 350 °C with an applied strain rate of the order of  $10^{-3} \text{ s}^{-1}$  are numerically analyzed.

## 2 Experimental Procedures

Ti–12Mo alloy was synthesized in a water-cooled Cu crucible by using cold crucible levitation melting technique with pure titanium (99.95 wt.%) and molybdenum (99.99 wt.%). Then, to ensure the uniformity of composition and remove the surface oxide layers of ingots, a homogenization treatment at 950 °C for 20 h followed by water quench and acidic bath (50 vol.% HF and 50 vol.% HNO<sub>3</sub>) was performed. After that, the ingots were cold-rolled into plates with a 90% thickness reduction, leading to a final thickness around 1 mm. Subsequently, tensile test specimens with a gauge size of  $10 \times 3 \times 1 \text{ mm}^3$  were cut from these rolled plates along the rolling direction, as shown in Fig. 1a. Furthermore, to analyze the deformation characteristics of specimens during tensile tests, a black and white contrast pattern was sprayed over the specimen surface prior to tests, as presented in the partial enlarged drawing of Fig. 1b. Finally, using Gleeble 3500 testing machine coupled with a digital image correlation technique, Ti–12Mo alloy tensile tests were performed at 350 °C with three different applied strain rates from the order of  $10^{-4} \text{ s}^{-1}$  to  $10^{-2} \text{ s}^{-1}$ . Note that, during the whole testing process, the maximum temperature gradient along the tensile direction measured by three thermocouples was less than 8.5% (Fig. 1c), and the temperature fluctuation of each thermocouple was maintained within 2 °C. Hence, the experimental tests can be regarded as isothermal tensile tests within the gauge size. Additionally, the corresponding engineering stress–strain curves were calculated and converted to the true stress–strain curves (Fig. 1d).

## 3 Modeling of the PLC Effect

### 3.1 Constitutive Model

Based on an elasto-visco-plastic frame work, McCormick's model [33–35] is employed to describe the PLC effect in Ti–12Mo alloy. Hereinto, the total deformation tensor is the sum of elastic and plastic strain tensors, as shown below:

$$\underline{\underline{\varepsilon}} = \underline{\underline{\varepsilon}}^e + \underline{\underline{\varepsilon}}^p, \quad \underline{\underline{\sigma}} = \underline{\underline{\zeta}} : \underline{\underline{\varepsilon}}^e \quad (1)$$

where  $\underline{\underline{\varepsilon}}^e$  and  $\underline{\underline{\varepsilon}}^p$  are respectively the elastic and plastic strain tensors,  $\underline{\underline{\sigma}}$  is the true stress tensor, and  $\underline{\underline{\zeta}}$  is the fourth-rank tensor of elastic modulus.

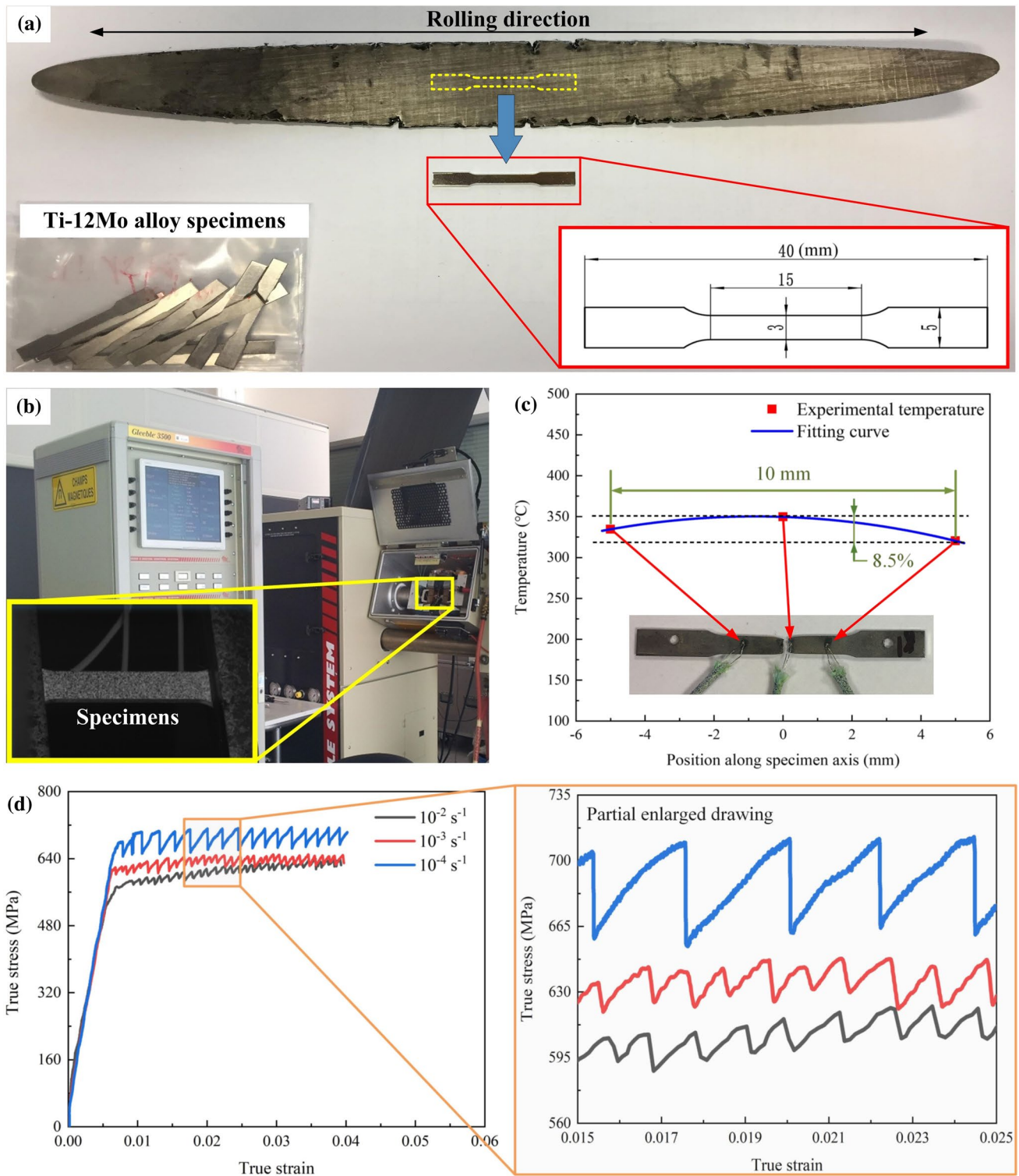


**Fig. 1** Ti-12Mo alloy specimens **a**, experimental equipment **b**, temperature gradient **c** and true stress–strain curves with partial enlarged drawing **d**

Moreover, the yield function is defined as:

$$f(\underline{\sigma}, p, t_a) = \sigma_{eq} - R(p) - R_a(p, t_a), \quad \sigma_{eq} = \sqrt{\frac{3}{2} \underline{s} : \underline{s}} \quad (2)$$

where  $\sigma_{eq}$  denotes the equivalent stress,  $R(p)$  means the strain hardening,  $R_a(p, t_a)$  is the yield stress,  $p$  is the equivalent plastic strain,  $t_a$  is an internal variable considering the ageing contribution to the yield stress, and  $\underline{s}$  is the deviatoric part of the stress tensor. Hereinto,  $R(p)$  can be defined as:

$$R(p) = Q(1 - \exp(-bp)) \quad (3)$$

where  $Q$  and  $b$  are hardening parameters.

Furthermore, the yield stress  $R_a(p, t_a)$  is written as:

$$R_a(p, t_a) = R_0 + P_1 C_m (1 - \exp(-P_2 p^\alpha t_a^n)) \quad (4)$$

where  $R_0$  is related to the initial yield stress,  $P_1 C_m$  corresponds to the stress drop magnitude,  $C_m$  denotes the concentration of  $\omega$  phase particles around the dislocation and its value is assumed as 1.  $P_2$ ,  $\alpha$  and  $n$  are related to the saturation rate, and the evolution equation of ageing time  $t_a$  is shown as below:

$$\dot{t}_a = \frac{t_w - t_a}{t_w}, \quad t_w = \frac{w}{\dot{p}} \quad (5)$$

where  $t_w$  denotes the mean waiting time of dislocations,  $w$  is the increment of plastic strain generated when all the stopped dislocations overcome the obstacles, and  $\dot{p}$  is the equivalent plastic strain rate calculated by the following viscoplastic hyperbolic flow rule.

$$\dot{p} = \dot{p}_0 \sinh\left(\frac{\langle f(\underline{\sigma}, p, t_a) \rangle}{K}\right) \quad (6)$$

where the bracket  $\langle f(\underline{\sigma}, p, t_a) \rangle$  means the maximum value between  $f(\underline{\sigma}, p, t_a)$  and 0,  $\dot{p}_0$  and  $K$  are material parameters.

Note that, prior to the critical plastic strain of the PLC effect, the equivalent plastic strain rate  $\dot{p}$  is nearly constant as increasing the plastic deformation. Therefore, the explicit expression of  $t_a$  in Eq. (5) can be expressed as a function of  $p$  [27]:

$$t_a(p) = \frac{\omega}{\dot{p}} \left(1 - \exp\left(-\frac{p}{\omega}\right)\right) + \frac{R_0}{E\dot{p}} \exp\left(-\frac{p}{\omega}\right) \quad (7)$$

Finally, coupling above equations, the homogeneous solution of stress  $\sigma$  can be written as:

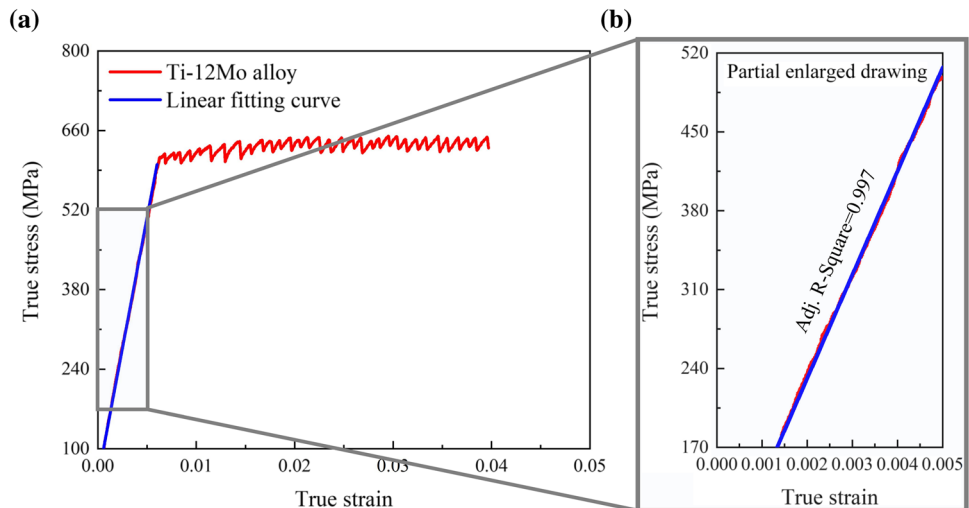
$$\sigma = K \operatorname{arcsinh} h\left(\frac{\dot{p}}{\dot{p}_0}\right) + R_0 + Q(1 - \exp(-bp)) + P_1 C_m (1 - \exp(-P_2 p^\alpha t_a(p)^n)) \quad (8)$$

### 3.2 Material Parameter Identification

In above equations, 13 material parameters need to be determined considering elastic and plastic deformation. The identification methods are presented in details below.

For elastic part of the strain in Ti-12Mo alloy, it is regarded as linear variation. Young’s Modulus ( $E$ ) can be obtained by linear fitting the experimental true stress–strain curve in the stress range [100–400 MPa], as shown in Fig. 2a. The result indicates that the linear fitting curve shows a good agreement with the experimental one with the adjusted R-squared=0.997 (Fig. 2b), and the value of  $E$  is 92.890 GPa. Moreover, with the same tensile testing conditions, the value of  $E$  reported by literature [8] is about 92 GPa, which further verifies the validity and accuracy of

**Fig. 2** Identification of Young’s Modulus of Ti-12Mo alloy **a** with partial enlarged drawing **b**



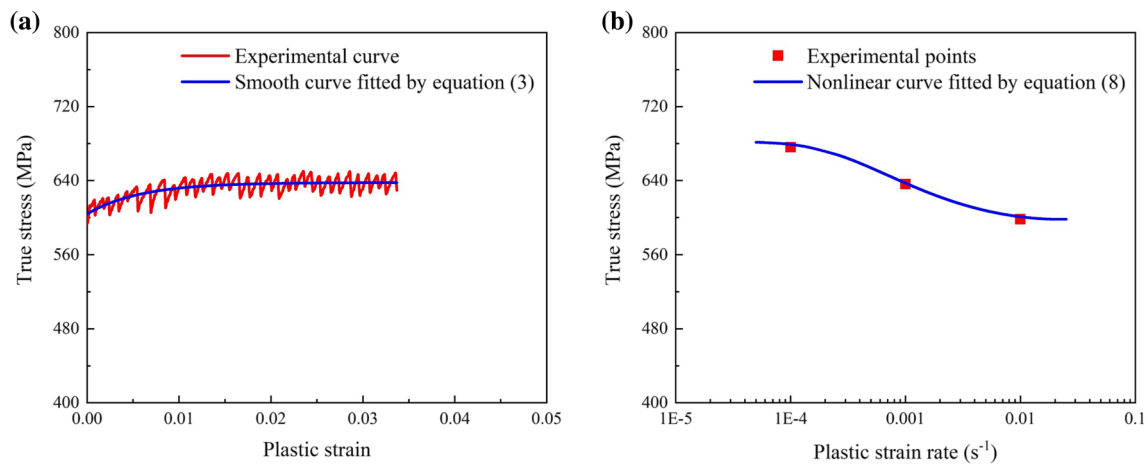


**Fig. 3** Identification methods for  $Q$ ,  $b$  and  $\sigma_y$  **a** as well as  $K$ ,  $\dot{p}_0$ ,  $P_1$ ,  $P_2$  and  $\alpha$  **b** of Ti-12 Mo alloy

**Table 1** Material parameters for modeling the PLC effect in Ti-12Mo alloy

Parameters	Units	Values
$E$	GPa	92.890
$\nu$	–	0.33 [36]
$R_0$	MPa	555
$Q$	MPa	27.075
$b$	–	220.458
$K$	MPa	15
$\dot{p}_0$	s <sup>-1</sup>	0.05
$P_1$	MPa	100
$P_2$	s <sup>-n</sup>	15
$C_m$	%	1
$\alpha$	–	0.36
$w$	–	10 <sup>-4</sup> [35]
$n$	–	0.66 [30]

the fitting result. Besides, Poisson’s ratio ( $\nu$ ) of Ti-12Mo alloy is 0.33, referring to [36].

Then, for the plastic part of Ti-12Mo alloy, the true stress-plastic strain curve of Ti-12Mo alloy is fitted by  $\sigma = \sigma_y + Q(1 - \exp(-bp))$  with Levenberg Marquardt iteration algorithm [31], as presented in Fig. 3a. It can be seen that the smooth curve effectively describes the hardening trend of the experimental curve, and the fitting parameters  $\sigma_y$ ,  $Q$  and  $b$  are respectively 607.854 MPa, 27.075 MPa and 220.458. Moreover, according to literatures [30, 35], three parameters ( $n$ ,  $w$  and  $C_m$ ) in Eqs. (4) and (5) are determined, whose values respectively are 0.66, 0.0001 and 1. Furthermore, in order to identify  $R_0$ , viscous ( $K$ ,  $\dot{p}_0$ ) and ageing ( $P_1$ ,  $P_2$ ,  $\alpha$ ) parameters, tensile tests at 350 °C with three different applied strain rates from the order of 10<sup>-4</sup> s<sup>-1</sup> to 10<sup>-2</sup> s<sup>-1</sup> are performed (Fig. 1d). Thereafter, from experimental results, true stress values at  $p = 0.02$  under each strain rates are measured and depicted as red points in Fig. 3b.

Subsequently, using the same iteration method as mentioned above, these points are fitted by Eq. (8). It can be seen that the nonlinear fitting curve is highly consistent with experimental data, which can prove the validity of the fitting results. Finally, the corresponding parameters ( $R_0$ ,  $K$ ,  $\dot{p}_0$ ,  $P_1$ ,  $P_2$ ,  $\alpha$ ) and aforementioned calibrated parameters ( $E$ ,  $\nu$ ,  $Q$ ,  $b$ ,  $n$ ,  $w$ ,  $C_m$ ) are summarized and listed in Table 1.

### 3.3 FE Validation

In contrast to explicit solution techniques, the implicit method can analyze static and quasi-static events easily and accurately, due to the reason that it is unconditionally stable with respect to the size of the time increment [37]. Therefore, to simulate the PLC effect in Ti-12Mo alloy, the above constitutive model with calibrated material parameters presented in Table 1 was implemented into Abaqus 6.14 finite element software as an external subroutine, using an implicit scheme. Figure 4a shows the schematic diagram of Ti-12Mo alloy uniaxial tensile tests. To simplify the model and improve computational efficiency, only the middle part of tensile test specimen with the size of 15 × 3 × 1 mm<sup>3</sup> was employed for 3D FE modelling. Figure 4b shows the established 3D FE model with geometric dimensions, boundary conditions and mesh details. Specifically, all the displacements and rotations on the left side of the FE model were restricted by using an encastre type boundary condition, and a constant velocity was applied to the right side. Moreover, a fixed increment size (10<sup>-4</sup>) was employed. Note that, to stabilize the simulations, the increment size can be further reduced when stress perturbation occurs. Furthermore, for mesh details, it should be pointed out that the element size was defined as 0.25 × 0.25 × 0.25 mm<sup>3</sup>, and eight node solid elements with reduced integration and enhanced hourglass control (C3D8R) were used for the FE model to avoid zero

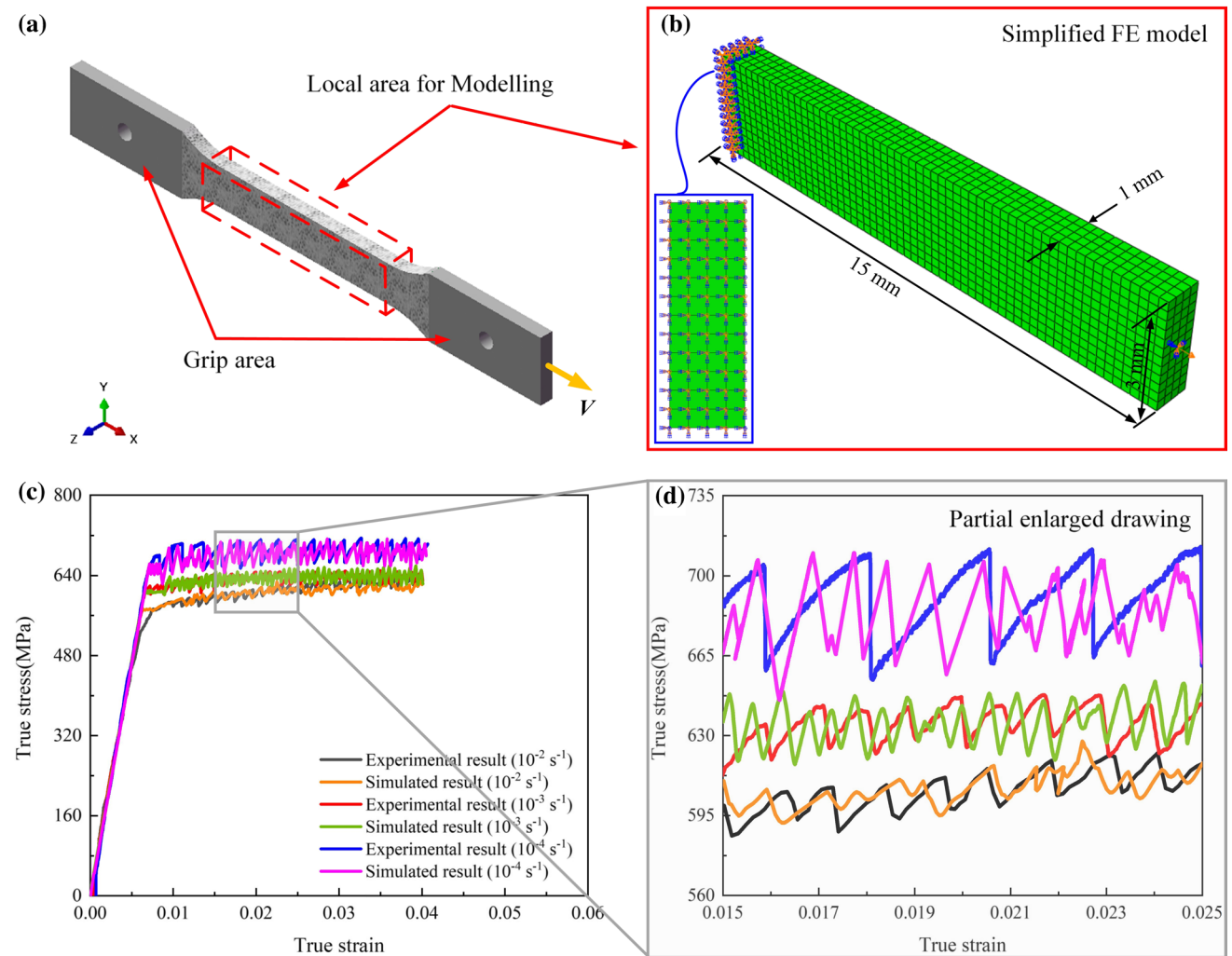


**Fig. 4** Schematic diagram of uniaxial tensile tests **a**, 3D simplified FE model with geometric dimensions, boundary conditions and mesh details **b**, and the comparison of simulated and experimental results at different strain rates **c** as well as partial enlarged drawing **d**

energy modes. The simulation process spends about 96 h, which was performed on a computer with Intel core i7-10700 k and 64 GB RAM. Figure 4c shows the overall comparison of simulated and experimental results at three different strain rates. It can be seen from Fig. 4d that although the simulated stress drop frequency is higher than the experimental ones influenced by  $t_a$ , the stress levels are well predicted for both elastic and plastic regions and the maximum error on the value of average stress drop magnitude is less than 9.1%, which is obtained by  $e = (\Delta\sigma_{e-average} - \Delta\sigma_{s-average}) / \Delta\sigma_{e-average}$ . Hereinto,  $e$  denotes the error between the experimental and simulated results,  $\Delta\sigma_{e-average}$  and  $\Delta\sigma_{s-average}$  are respectively experimental and simulated average stress drop magnitudes calculated by  $\Delta\sigma_{average} = \sum_1^N (\Delta\sigma) / N$ . Hence, it can be concluded that the 3D FE model with the constitutive model and material

parameters mentioned in Sects. 3.1 and 3.2 is valid for simulating the PLC effect in Ti-12Mo alloy.

## 4 Results and Discussion

### 4.1 Strain–Time Curve and Strain Localization

Figure 5a shows the variation of true strain versus the time at the constant simulated tensile velocity (0.01 mm/s). For each time, the true strain is calculated by  $\epsilon = \ln(1 + \Delta L / L_1)$  [39], where  $\Delta L$  is the displacement difference of two points ( $P_1$  and  $P_3$ ) and  $L_1$  is the gauge length (10 mm). It can be obtained from Fig. 5a that the slope of the true strain–time curve is about  $0.00095 \text{ s}^{-1}$ , which is in accordance with the experimental strain rate (about  $0.0011 \text{ s}^{-1}$ ). Moreover, Fig. 5b presents the variation of  $p$  with the increase of the

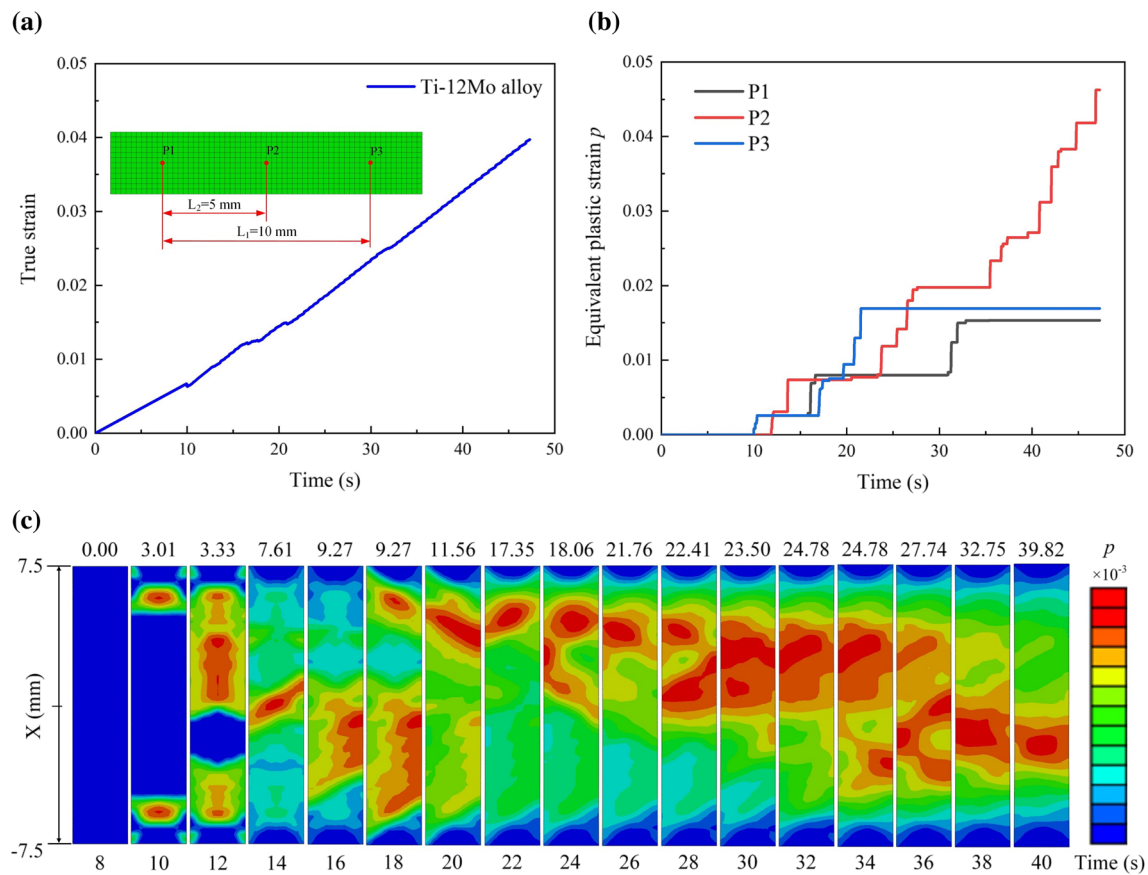


**Fig. 5** True strain–time curve **a**, equivalent plastic strain–time curves of three selected points **b**, and the distribution of equivalent plastic strain in Ti-12Mo alloy simulated tensile procedure **c**

time at three points ( $P_1$ ,  $P_2$  and  $P_3$ ). It can be seen that the  $p$  values of three points are 0 prior to 10 s. This is because this tensile process mainly results in elastic deformation within the tensile specimen. Furthermore, after 10 s, staircase behaviors are observed as increasing the tensile time, which is similar to the results reported by Mansouri et al. [31] and Benallal et al. [34]. This phenomenon is mainly attributed to the heterogeneous deformation during the tensile procedure. Finally, it can be found that the largest  $p$  value at  $P_2$  (about 0.045) is more than twice as big as the largest ones at  $P_1$  and  $P_3$ , although the deformation beginning time of the former is later than the ones of the latter. This phenomenon can be explained by the reason that the localized plastic deformation firstly occurs at both ends of the tensile specimen, then gradually transfers to its middle part, and eventually stays at this place with the increase of the time, as shown in Fig. 5c. Note that, to provide a maximum contrast, the color scale presented in Fig. 5c is independent for each frame, based on the instantaneous maximum and minimum values of equivalent plastic strain. The corresponding maximum equivalent

plastic strain and time are indicated over and under each frame, respectively.

## 4.2 Stress–Time Curve and PLC Band Propagation

Figure 6a shows the variation of true stress versus the time at the constant simulated tensile velocity (0.01 mm/s). For each time, the true stress is obtained by  $\sigma = F(1 + \Delta L/L_1)/A_0$ , where  $F$  is the tensile force and  $A_0$  is the initial cross-sectional area of the tensile specimen (3 mm<sup>2</sup>). It can be observed from Fig. 6a that the true stress shows serrated flow at the level of 620 MPa after a linear rise when the tensile time increases to the value of 10 s. This phenomenon is related to the transformation from elastic to plastic deformation. Moreover, in order to analyze the propagation characteristics of the PLC band, the partial enlarged drawing of the serrated part and the corresponding PLC band at the marked valley of the stress flow are depicted in Fig. 6b and c, respectively. Like Fig. 5c, the color scale presented in Fig. 6c is also independent for each frame with the corresponding maximum strain rate and time indicated over and under each frame. It can be

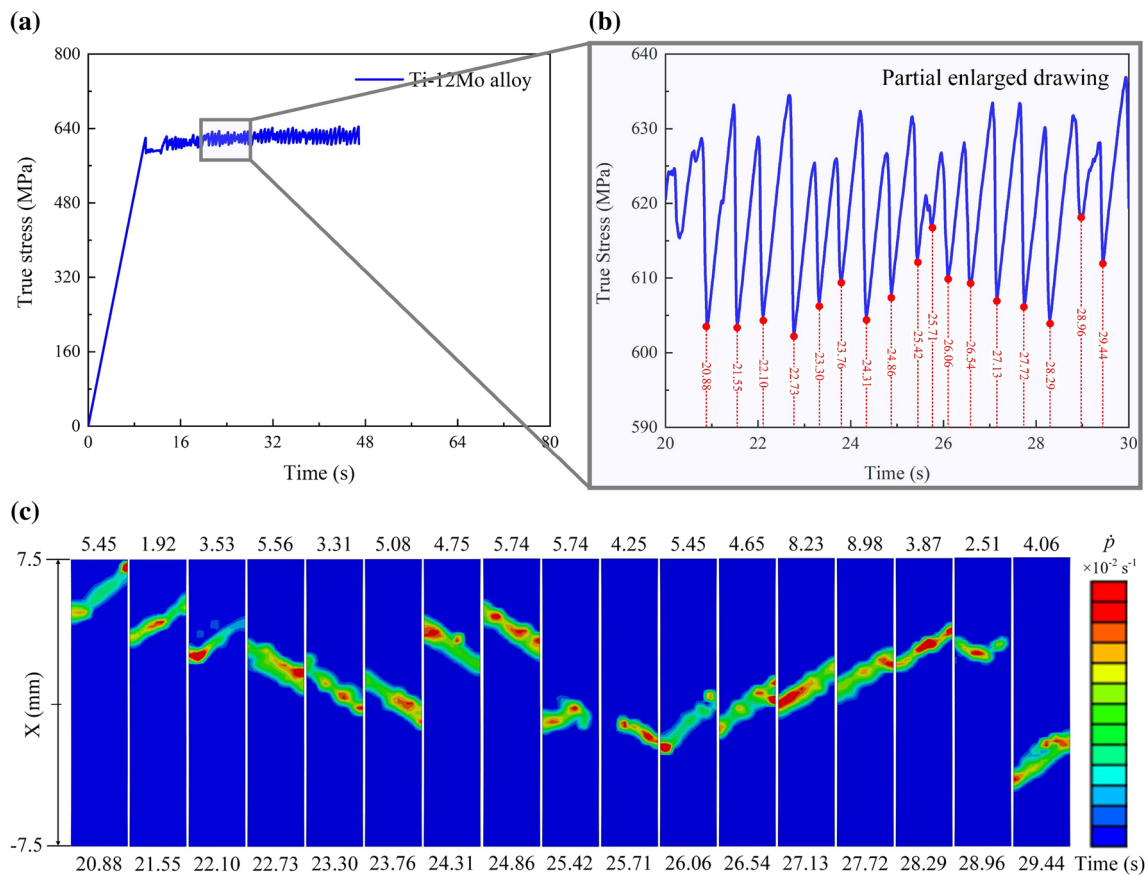


**Fig. 6** True stress-time curve **a**, partial enlarged drawing of selected area **b** and propagation of PLC bands in Ti-12Mo alloy simulated tensile procedure **c**

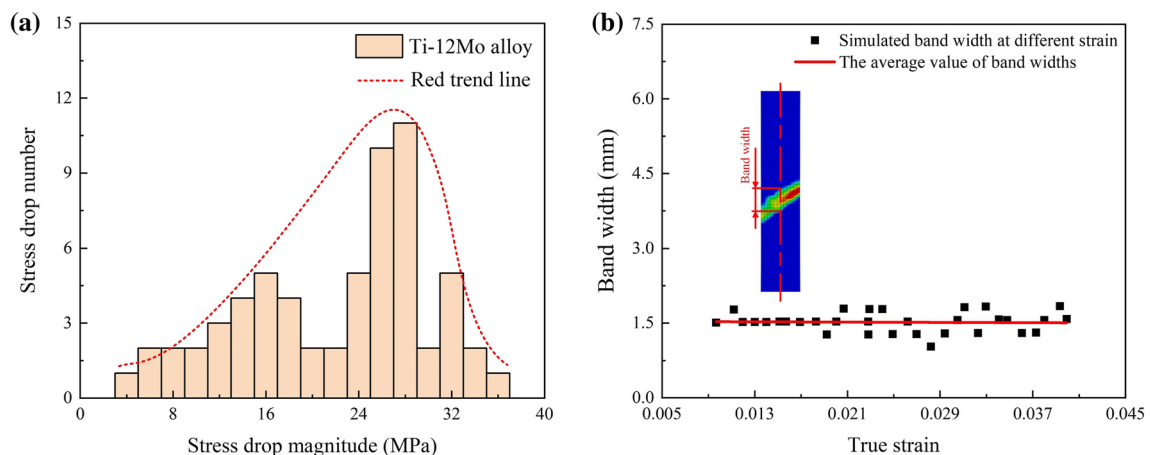


**Fig. 7** Stress drop magnitude distribution **a** and the PLC band width evolution **b** in Ti-12Mo alloy simulated tensile procedure

observed from Fig. 6c that the hopping propagation of the PLC band appears with the increase of the tensile time, which indicates that a type B propagation will occur at 350 °C with the applied strain rate of the order of  $10^{-3} \text{ s}^{-1}$  in Ti-12Mo alloy tensile procedure. This phenomenon is

closely consistent to the results reported by Luo et al. [9, 10], who investigated the propagation characteristics of the PLC bands in Ti-xMo alloys by using a digital image correlation method. Besides, like the angle variations of the PLC bands in an AlMg alloy reported by Yuzbekova et al.



[11], it can be found in Ti-12Mo alloy that the inclined angle of the PLC band also changes during the PLC band propagation process. This phenomenon is mainly related to variations of stress conditions influenced by stress drop magnitudes.

### 4.3 Stress Drop Magnitude and PLC Band Width

To quantitatively analyze the distribution of stress drop magnitudes in Ti-12Mo alloy tensile procedure, the variation of stress drop number versus the stress drop magnitude at the constant simulated tensile velocity (0.01 mm/s) is presented in Fig. 7a. Hereinto, the stress drop magnitude is measured from simulated true stress–strain curve depicted in Fig. 4b. It can be seen from Fig. 7a that the maximum and minimum values of stress drop magnitudes are about 36 and 4 MPa, respectively. These values are slightly higher than experimental ones, whose maximum and minimum values are respectively about 34 and 2 MPa. Moreover, the simulated and experimental values of average stress drop magnitudes are calculated by  $\Delta\sigma_{average} = \sum_1^N (\Delta\sigma)/N$  [10], which are respectively 21.2 and 19.7 MPa. Furthermore, it can be observed from the red trend line that the distribution of stress drop magnitudes follows a normal distribution and its peak value is in the range of 26–28 MPa. Besides, to quantitatively reflect strain localization characteristics, the variation of the PLC band width with the increase of true strain is described in Fig. 7b. Note that, using the same measurement method reported by Sene et al. [38], the PLC band width is measured on the central axis of the specimen along the tensile direction. It can be observed from Fig. 7b that the value of the PLC band width slightly fluctuates with the increase of true strain, and its average value is about 1.5 mm.

This phenomenon shows a good agreement with our previous experimental results (about 1.35 mm) [9].

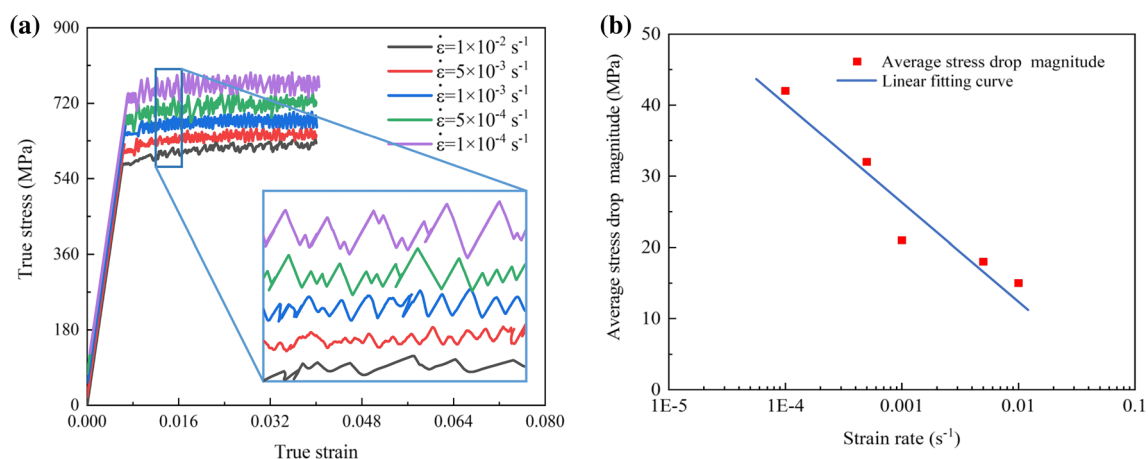
### 4.4 Influence of Strain Rates on the Average Stress Drop Magnitude

Figure 8a shows the simulated stress–strain curves at different strain rates with the partial enlarged drawing. Note that, these curves are shifted sequentially along the positive direction of the Y axis by 20 MPa for clarity. It can be seen that the stress level rises with the decrease of strain rates. Moreover, to quantitatively analyze the average stress drop magnitude in Fig. 8a, the evolution of average stress drop magnitudes with the increase of strain rates is depicted in Fig. 8b. It can be observed that the value of the average stress drop magnitude decreases from 42 to 15 MPa as increasing the strain rate from  $10^{-4} \text{ s}^{-1}$  to  $10^{-2} \text{ s}^{-1}$ . This phenomenon can be explained by the reason that a lower strain rate results in a longer ageing time ( $t_a$ ), further leading to a stronger interaction between  $\omega$  phase particles and mobile dislocations, thereby causing the increase of the average stress drop magnitude.

## 5 Conclusions

In this paper, McCormick's model implemented in Abaqus 6.14 software is used to simulate the spatiotemporal characteristics of the PLC effect in Ti-12Mo alloy tensile procedure and verified by experiments. The conclusions are summarized as following:

- (1) McCormick's model with calibrated material parameters can well predict the spatiotemporal behaviors



**Fig. 8** Simulated true stress–strain curves at different strain rates **a** and the evolution of average stress drop magnitudes with the increase of strain rates **b**

of the PLC effect in Ti-12Mo alloy tensile procedure, especially in terms of stress drop magnitudes and PLC band widths. Moreover, the identification methods of corresponding material parameters and the 3D FE modeling procedure are presented in details, which can provide a significant guidance for the simulation of PLC effect in other materials.

- (2) For the temporal behaviors of the PLC effect in Ti-12Mo alloy, strain staircases are observed as increasing the tensile time, which can be attributed to the strain localization. Moreover, for its spatial behaviors, the hopping propagation of the PLC band appears and the inclined angle of the PLC band changes in Ti-12Mo alloy tensile procedure. These phenomena are mainly related to the variation of stress drop magnitudes.
- (3) The average stress drop magnitude decreases with the increase of strain rates. Moreover, the distribution of simulated stress drop magnitudes at velocity = 0.01 mm/s follows a normal distribution and its peak value is in the range of 26–28 MPa. Furthermore, the PLC band width slightly fluctuates with the increase of true strain and its average value is about 1.5 mm. Besides, to further numerically analyze the temperature and strain rate ranges for the occurrence of the PLC effect in Ti-12Mo alloy, the material parameters of McCormick's model will be identified as a function of temperature in the future work.

**Acknowledgements** This work was supported by the Hubei Provincial Natural Science Foundation of China (Grant no. 2020CFB115).

**Author contribution** SL: Conceptualization, Methodology, Software, Writing—Original Draft. YJ: Investigation, Validation, Writing—original draft. ST: Data curation, Writing- review & editing. PC: Data curation, Writing—review & editing. LZ: Supervision, Writing—Review & Editing.

## Declarations

**Conflict of interest** The authors declare that they have no known competing financial interests or personal relationships that could have appeared to influence the work reported in this paper.

## References

1. S.Y. Luo, J.N. Yao, J. Li, H. Du, H.Y. Liu, F.P. Yu, Influence of forging velocity on temperature and phases of forged Ti-6Al-4V turbine blade. *J. Mater. Res. Technol.* **9**(6), 12043–12051 (2020)
2. S. Gurel, M.B. Yagci, D. Canadinc, G. Gersein, B. Bal, H.J. Maier, Fracture behavior of novel biomedical Ti-based high entropy alloys under impact loading. *Mater. Sci. Eng. A* **803**(28), 140456 (2021)
3. P.Y. Li, X.D. Ma, T. Tong, Y.S. Wang, Microstructural and mechanical properties of  $\beta$ -type Ti-Mo-Nb biomedical alloys with low elastic modulus. *J. Alloy. Compd.* **815**, 152412 (2020)
4. S.E. Haghighi, H. Attar, I.V. Okulov, M.S. Dargusch, D. Kent, Microstructural evolution and mechanical properties of bulk and porous low-cost Ti-Mo-Fe alloys produced by powder metallurgy. *J. Alloy. Compd.* **853**(6), 156768 (2021)
5. W. Xu, M. Chen, X. Lu, D.W. Zhang, H.P. Singh, J.S. Yu, Y. Pan, X.H. Qu, C.Z. Liu, Effects of Mo content on corrosion and tribocorrosion behaviours of Ti-Mo orthopaedic alloys fabricated by powder metallurgy. *Corros. Sci.* **168**, 108557 (2020)
6. N. Kang, Y.L. Li, X. Lin, E.H. Feng, W.D. Huang, Microstructure and tensile properties of Ti-Mo alloys manufactured via using laser powder bed fusion. *J. Alloy. Compd.* **771**, 877–884 (2019)
7. F. Sun, F. Prima, T. Gloriant, High-strength nanostructured Ti-12Mo alloy from ductile metastable beta state precursor. *Mater. Sci. Eng. A* **527**(16–17), 4262–4269 (2010)
8. S. Banerjee, U.M. Naik, Plastic instability in an omega forming Ti-15% Mo alloy. *Acta Mater.* **44**(9), 3667–3677 (1996)
9. S.Y. Luo, P. Castany, S. Thuillier, M. Huot, Spatiotemporal characteristics of Portevin-Le Chatelier effect in Ti-Mo alloys under thermo-mechanical loading. *Mater. Sci. Eng. A* **733**, 137–143 (2018)
10. S.Y. Luo, P. Castany, S. Thuillier, Microstructure, thermo-mechanical properties and Portevin-Le Chatelier effect in metastable  $\beta$  Ti-xMo alloys. *Mater. Sci. Eng. A* **755**, 61–70 (2019)
11. D. Yuzbekova, A. Mogucheva, D. Zhemchuzhnikova, T. Lebedkina, M. Lebyodkin, R. Kaibyshev, Effect of microstructure on continuous propagation of the Portevin-Le Chatelier deformation bands. *Int. J. Plast.* **96**, 210–226 (2017)
12. K. Chihab, Y. Estrin, L.P. Kubin, J. Vergnol, The kinetics of the Portevin-Le Chatelier bands in an Al-5at%Mg alloy. *Scr. Metal.* **21**(2), 203–208 (1987)
13. H.A. Amokhtar, S. Boudrahem, C. Fressengeas, Spatiotemporal aspects of jerky flow in Al-Mg alloys, in relation with Mg content. *Scr. Mater.* **54**(12), 2113–2118 (2006)
14. R. Zhang, C.G. Tian, C.Y. Cui, Y.Z. Zhou, X.F. Sun, Portevin-Le Châtelier effect in a wrought Ni-Co based superalloy. *J. Alloy. Compd.* **818**, 152863 (2020)
15. S.Y. Chen, W.D. Li, F.C. Meng, Y. Tong, H. Zhang, K.K. Tseng, J.W. Yeh, Y. Ren, F. Xu, Z.G. Wu, P.K. Liaw, On temperature and strain-rate dependence of flow serration in HfNbTaTiZr high-entropy alloy. *Scr. Mater.* **200**(5), 113919 (2021)
16. D. Yuzbekova, A. Mogucheva, Y. Borisova, R. Kaibyshev, On the mechanisms of nucleation and subsequent development of the PLC bands in an AlMg alloy. *J. Alloy. Compd.* **868**, 159135 (2021)
17. C.Y. Cui, R. Zhang, Y.Z. Zhou, X.F. Sun, Portevin-Le Châtelier effect in wrought Ni-based superalloys: experiments and mechanisms. *J. Mater. Sci. Technol.* **51**, 16–31 (2020)
18. Y. Choi, J.J. Ha, M.G. Lee, Y.P. Korkolis, Effect of plastic anisotropy and Portevin-Le Chatelier bands on hole-expansion in AA7075 sheets in -T6 and -W tempers. *J. Mater. Process. Technol.* **296**, 117211 (2021)
19. M. Mehenni, H.A. Amokhtar, C. Fressengeas, Spatiotemporal correlations in the Portevin-Le Chatelier band dynamics during the type B-type C transition. *Mater. Sci. Eng. A* **756**, 313–318 (2019)
20. K.C. Yu, L.G. Hou, M.X. Guo, D.Y. Li, D.N. Huang, L.Z. Zhuang, J.S. Zhang, P.D. Wu, A method for determining r-value of aluminum sheets with the Portevin-Le Chatelier effect. *Mater. Sci. Eng. A* **814**, 141246 (2021)
21. Y.K. Liu, Y.L. Cai, C.G. Tian, G.L. Zhang, G.M. Han, S.H. Fu, C.Y. Cui, Q.C. Zhang, Experimental investigation of a

- Portevin-Le Chatelier band in Ni-Co-based superalloys in relation to  $\gamma'$  precipitates at 500 °C. *J. Mater. Sci. Technol.* **45**, 35–41 (2020)
22. B. Reyne, P.Y. Manach, N. Moës, Macroscopic consequences of Piobert-Lüders and Portevin-Le Chatelier bands during tensile deformation in Al-Mg alloys. *Mater. Sci. Eng. A* **746**, 187–196 (2019)
  23. M. Callahan, O. Hubert, F. Hild, A. Perlade, J.H. Schmitt, Coincidence of strain-induced TRIP and propagative PLC bands in medium Mn steels. *Mater. Sci. Eng. A* **704**, 391–400 (2017)
  24. L.P. Kubin, Y. Estrin, The Portevin-Le Chatelier effect in deformation with constant stress rate. *Acta Metall.* **33**(3), 397–407 (1985)
  25. P.G. McCormick, Theory of flow localisation due to dynamic strain ageing. *Acta Metall.* **36**(12), 3061–3067 (1988)
  26. S. Zhang, P.G. McCormick, Y. Estrin, The morphology of Portevin-Le Chatelier bands: finite element simulation for Al-Mg-Si. *Acta Mater.* **49**(6), 1087–1094 (2001)
  27. M. Mazière, J. Besson, S. Forest, B. Tanguy, H. Chalons, F. Vogel, Numerical modelling of the Portevin-Le Chatelier effect. *Eur. J. Comput. Mech.* **17**(5–7), 761–772 (2008)
  28. P.Y. Manach, S. Thuillier, J.W. Yoon, J. Coër, H. Laurent, Kinematics of Portevin-Le Chatelier bands in simple shear. *Int. J. Plast.* **58**, 66–83 (2014)
  29. L.Z. Mansouri, J. Coër, S. Thuillier, H. Laurent, P.Y. Manach, Investigation of Portevin-Le Chatelier effect during Erichsen test. *Int. J. Mater. Form.* **13**(5), 687–697 (2019)
  30. J. Belotteau, C. Berdin, S. Forest, A. Parrot, C. Prioul, Mechanical behavior and crack tip plasticity of a strain aging sensitive steel. *Mater. Sci. Eng. A* **526**(1–2), 156–165 (2009)
  31. L.Z. Mansouri, S. Thuillier, P.Y. Manach, Thermo-mechanical modeling of Portevin-Le Chatelier instabilities under various loading paths. *Int. J. Mech. Sci.* **115**, 676–688 (2016)
  32. C. Moon, S. Thuillier, J. Lee, M.G. Lee, Mechanical properties of solution heat treated Al-Zn-Mg-Cu (7075) alloy under different cooling conditions: analysis with full field measurement and finite element modeling. *J. Alloy. Compd.* **856**, 158180 (2020)
  33. S. Graff, H. Dierke, S. Forest, H. Neuhäuser, J.L. Strudel, Finite element simulations of the portevin-Le Chatelier effect in metal-matrix composites. *Philos. Mag.* **88**(28–29), 3389–3414 (2008)
  34. H. Dierke, F. Krawehl, S. Graff et al., Portevin-LeChatelier effect in Al-Mg alloys: influence of obstacles—experiments and modelling. *Comput. Mater. Sci.* **39**(1), 106–112 (2007)
  35. A. Benallal, T. Berstad, T. Børvik, O.S. Hopperstad, I. Koutiri, R.N.D. Codes, An experimental and numerical investigation of the behaviour of AA5083 aluminium alloy in presence of the Portevin-Le Chatelier effect. *Int. J. Plast.* **24**(10), 1916–1945 (2008)
  36. T. Furuhashi, T. Makino, Y. Idei, H. Ishigaki, A. Takada, T. Maki, Morphology and crystallography of  $\alpha$  precipitates in  $\beta$  Ti-Mo binary alloys. *Mater. Trans. JIM* **39**(1), 31–39 (1998)
  37. A.M. Prior, Applications of implicit and explicit finite element techniques to metal forming. *J. Mater. Process. Technol.* **45**(1–4), 649–656 (1994)
  38. N.A. Sene, P. Balland, K. Bouabdallah, Experimental study of Portevin-Le Chatelier bands on tensile and plane strain tensile tests. *Arch. Civ. Mech. Eng.* **18**(1), 94–102 (2018)
  39. S.W. Tu, X.B. Ren, J.Y. He, Z.L. Zhang, Stress-strain curves of metallic materials and post-necking strain hardening characterization: a review. *Fatigue Fract. Eng. Mater. Struct.* **43**(1), 3–19 (2020)

**Publisher's Note** Springer Nature remains neutral with regard to jurisdictional claims in published maps and institutional affiliations.